Darcy scale modelling of smouldering: impact of heat loss

Victor Pozzobon[1] ✉, **Baud Germain**[1], **Sylvain Salvador**[1], **and Gerald Debenest**[2]

[1]Université de Toulouse, centre RAPSODEE, UMR CNRS 5302, Mines Albi, Campus Jarlard, route de Teillet, 81013 CT Albi Cédex 09, France
[2]Institut de Mécanique des Fluides de Toulouse, 31400, Toulouse, France

Modelling the propagation of smoldering fronts with forced air feeding in a porous medium remains a challenge to science. One of the main difficulties is to describe the carbon oxidation reaction that supports this self-sustained process. Pore scale approaches are required to tackle this complex coupled heat and mass transfer problem with chemistry. They nevertheless require high computation effort and still miss experimental validation. Furthermore, the heat loss at the walls of the cells inherent to every laboratory scale system adds another level of complexity in the understanding of the coupling between the phenomena at stake. Indeed, it induces a non homogeneous temperature field throughout the system. In this paper, a 2D Darcy scale model is developed and validated by confrontation with experimental results from the literature, covering wide ranges of carbon content of the medium and forced air velocity. A reasonable description of the front temperature, velocity and non-consumption oxygen amount is reached. The model finally enables to bring understanding of the impact of heat loss which controls front shape and stability near the system walls.

Smoldering | Homogeneous porous medium | Modelling

Correspondence: ***victor.pozzobon@mines-albi.fr***

1. Introduction

Smouldering is a process in which a combustion wave propagates through a porous medium. It is involved in many situations both naturally and in man-controlled processes. Energy applications (1, 2) but also environment science (3, 4) and forest management (5, 6) are classical areas of application.

The propagation of the combustion wave is a complex problem involving heat and mass transfer together with chemical reactions and sometimes phase changes. It is admitted that the energy required to enable the self-propagation of the wave is brought by the direct and flameless oxidation of some carbon in the medium. This carbon is most of the time the result of a previous solid fuel devolatilization that leads to the formation of volatile matters – gas and tars – and of a sometimes called fixed carbon. As the wave progresses, the endothermic drying of the medium is forced. If the medium contains carbonates, the endothermic decarbonation of the medium occurs when the temperature overpasses 800 °C approximately (7).

The description of these phenomena in numerical models remains a challenge to science. Theoretically, the structure of the filtration combustion front was analysed in 1D-geometry, like in the study of (8). Several others can be found depending on the methods, but also on the operating conditions, i.e., for instance cocurrent and countercurrent situations (9, 10). In all these studies, a simplified chemistry is assumed, usually first-order and Arrhenius-like reactions. Furthermore, the strong coupling existing between heat and mass transport with a complex, multi-step chemistry, depending on local scale thermochemical conditions, is not explicitly addressed. For instance, the wave temperature depends on the amount of heat released from carbon oxidation in the reacting zone. Several recent attempts have been done to study in-detail image of porous media, the dynamics and regime of such a wave at the pore scale in density variable conditions (11) or in non-dilatable situations (12). They clearly demonstrate, even using simplified chemistry, the competitive effect between residence time of oxygen in the front and the thermal equilibrium to maintain the combustion process. Increasing the flow rate could lead to unburnt carbon and then to transition in thermal wave temperature like in (13). In turn, the front velocity depends on a number of parameters. It is essentially governed by the stoichiometry of the carbon oxidation reaction with the fed oxygen. This nevertheless requires that the fraction of carbon actually oxidized and the fraction of oxygen actually consumed by the front - both of which depend on the front temperature - are well predicted.

Also, these transitions in thermal wave transport and combustion regimes affect the chemistry. Usually, we lump all the reactions representing the carbon oxidation process into a simplified model. This has been done in (14), but also in (15). A global description of this very complex process can be given as:

$$C + (1 - \frac{fr_{CO}}{2})\, O_2 \mapsto fr^{CO}\, CO + (1 - fr_{CO})\, CO_2 \lambda \quad \textbf{(1)}$$

Where fr_{CO} is the fraction of carbon that is oxidized into CO. The fr_{CO} parameter strongly affects the front velocity. Indeed the velocity varies by a factor of 2 when fr_{CO} changes from 0 to 1. The energy released at carbon oxidation increases from 110.5 kJ/mole for fr_{CO} = 1 to 393.5 kJ/mole when fr_{CO} = 0. This will also strongly impact the front temperature.

The prediction by models of the fr_{CO} value is a challenging task. This is due to the fact that final amount of CO and CO_2 observed depend on a number of parameters such as the air flow, the front temperature, the medium carbon content and the geometry of the medium particles. The primary formation of CO by the heterogeneous reaction of O_2 with solid carbon is admitted to be followed by homogeneous oxidation of CO into CO_2, but also by reaction of the formed

CO_2 with solid carbon. The chemical phenomena are coupled with transport phenomena that impact on gas mixing efficiency and on solid-gas contact time, as discussed in (16). Therefore, predicting fr_{CO} from a numerical model can only be tackled at the pore scale. This task remains complex and a review of the possible modelling approaches is presented in (17) that deals with the upscaling of such a problem from pore scale to Darcy scale.

In addition to this already complex situation, another inevitable phenomenon stacks: heat loss. Indeed, no experimental device is perfectly insulated. Heat loss lowers temperature having an impact on several local physical properties such as gas density, gas viscosity and even on the fr_{CO} parameter. This adds another level of complexity in the understanding of the coupling between the phenomena at stake. To summarize, the fact is that the literature does not propose a modelling approach with affordable computation time able to predict a carbon consuming front velocity and temperature, together with the amounts of unburnt carbon after the front passage and non-consumed oxygen. In addition, to our knowledge, none of the currently available models properly takes into account the heat loss. Heat loss are described as a volumetric sink term in 1D (15) or as a prescribed heat flux on the external boundary in 2D (18, 19). One should note that theses prescribed heat fluxes have to be experimentally monitored, then provided to the model, which hinders the model actual predictive culpabilities. Developing a model properly accounting for the heat loss – based on a simple description of carbon oxidation reaction - is the purpose of this paper. The global strategy is described below:

- a set of 12 experimental results was first established in a previous work (20). A situation as simple as possible was aimed at, developing a model medium containing only carbon in an inert matrix of alumina. Two parameters of primary importance were varied in ranges as large as possible: the carbon content between 2.30 and 3.58 % and the air flux by a factor of 10. Five experiments in extreme conditions were selected among them.

- a numerical model was developed in this work with the aim to describe the five experiments, properly accounting for the heat loos and keeping the description of carbon oxidation reaction as simple as possible.

The final confrontation of model to experiments will be done to obtain some of the important front characteristics. These depend on the operating conditions, mainly, flow rate and carbon concentration. We will demonstrate the ability of the numerical model to explain the impact of heat loss on the smouldering front.

2. Experimental device and experimental database

The combustion cell used to obtain the experimental data bank is described in detail in (20) (Fig. 1). Briefly, it consists of a stainless steel tube (91 mm diameter, 600 mm long) filled with a granular reactive porous medium. The tube was thermally insulated using a 50 mm thick Kaowool HS-45 insulating material, around the cylinder.

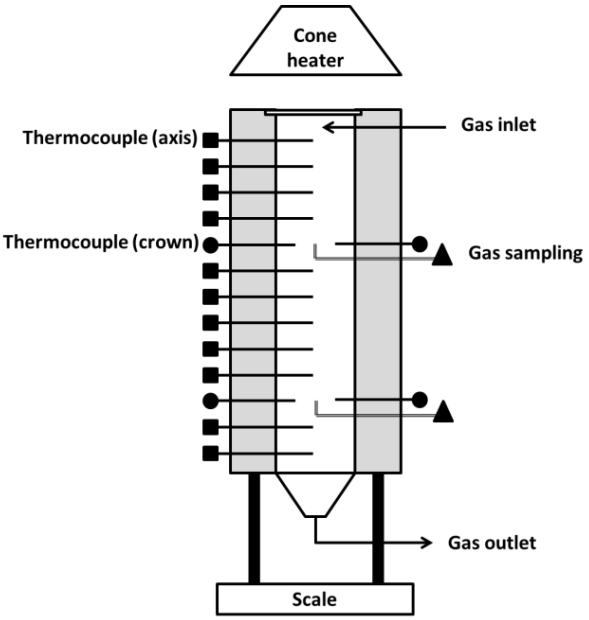

Fig. 1. Schematic of the experimental apparatus (20)

Air was fed from the top of the cell. Ignition was operated by irradiating the top of the bed with a high density radiative flux of 50 kW/m^2, through a quartz window. Smouldering was therefore operated in the forward configuration.

The reactive porous medium was specially developed to keep the situation as simple as possible. We use porous alumina spheres with diameters ranging from 1.25 to 3.15 mm. They were enriched with solid carbon in controlled amounts thanks to a procedure described in (20).

To serve as model validation benchmark, the results from five experiments were selected. In the first three experiments, the carbon content is varied from 2.30 to 3.58 % in mass. These values range from near extinction carbon content to the highest temperature the combustion cell was designed for (20). In the other experiments the air flux is varied between 21 and 210 mm/s above the bed at 20 °C. One of the points is common. Table 1 summaries the experimental conditions and main results for the selected experiments. It can be seen that the front temperature varies in a range as large as 709 °C - which is close to the known extinction temperature of 550 °C - up to 1465 °C. This last temperature is higher than the maximum cell design value and was unexpected. It counter-intuitively results from the incomplete consumption of oxygen by the front. As the fed air velocity was increased by a factor of 10, the front velocity increased from 5.2 to 30.4 mm/min. The ratio of 10 is not retrieved because of the incomplete consumption of oxygen by the front at high air velocity. The experimental velocity of the front is calculated from the time separating the front passage (i.e. maximum temperatures) at successive thermocouples along the cell axis. The stoichiometry of carbon consumption by the fed oxygen has been expressed by (21), from which the front

velocity can be expressed as a function of the experimental parameters (Eq. 2).

$$v_{frc} = \frac{v_g \rho_g}{M_g} Y_{O_2} fr_{Ooxi} \frac{M_C}{C \rho_{bed} fr_{Coxi} (1 - \frac{fr_{CO}}{2})} \quad \textbf{(2)}$$

This velocity is called theoretical front velocity in the paper, and will be used for stoichiometry checking purposes. It was shown that all of the experiments are in the reaction leading mode, where the chemical front propagates faster than the thermal front. Description of such regimes and others can be found in (8).

It was observed that all of the carbon was oxidized after the passage of the front, for all of the experiments. It was also observed in (20) that the temperature at the axis of the combustion cell are significantly higher than closed to the walls (1cm away from the walls). This indicates that significant heat losses occur at the cell walls. This will impact discussion on the choice of the model especially the discussion of 1D or 2D approach.

3. Numerical model

For the sake of simplicity and to investigate several effects, pore scale modelling was not considered here. Rather, a Darcy scale approach was adopted. As a consequence and as discussed before, it cannot be considered to predict the value of fr_{CO} from the model. Recent studies have not lead to this prediction even in (11), where a complete local scale model is used. The proposed approach here is to use in the model the values learnt from experiments, under the form of simple functions depending only on the front temperature and on air flux. The carbon combustion reaction is described globally following Eq. 1. We will describe this reaction through an Arrhenius formulation.

The experimental results suggest that important heat losses occur at the cell walls as pointed out before. Therefore, a 2D model was developed and not a simpler 1D model like in (15). As the insulating layer around the medium was taken into account, the model is indeed expected to bring insights to explain the observed radial temperature gradients and front curving.

The smouldering cell is described in two parts: the reaction medium and the surrounding insulating material. The reacting porous medium is described as a homogeneous domain governed by mass, heat and momentum conservation laws. Thermal transport equation will be solved simultaneously in the insulating shell. The case was taken as a 2D transient axisymmetrical case. A special care was put in choosing the boundary conditions which best described experimental operating conditions (Fig. 2).

3 1. Heat balance

According to the experimental conditions, an increase in the flow rate could lead to local non equilibrium (22). According to (23), combustion in porous media occurs in the large range of time and length scale. As a consequence, it usually

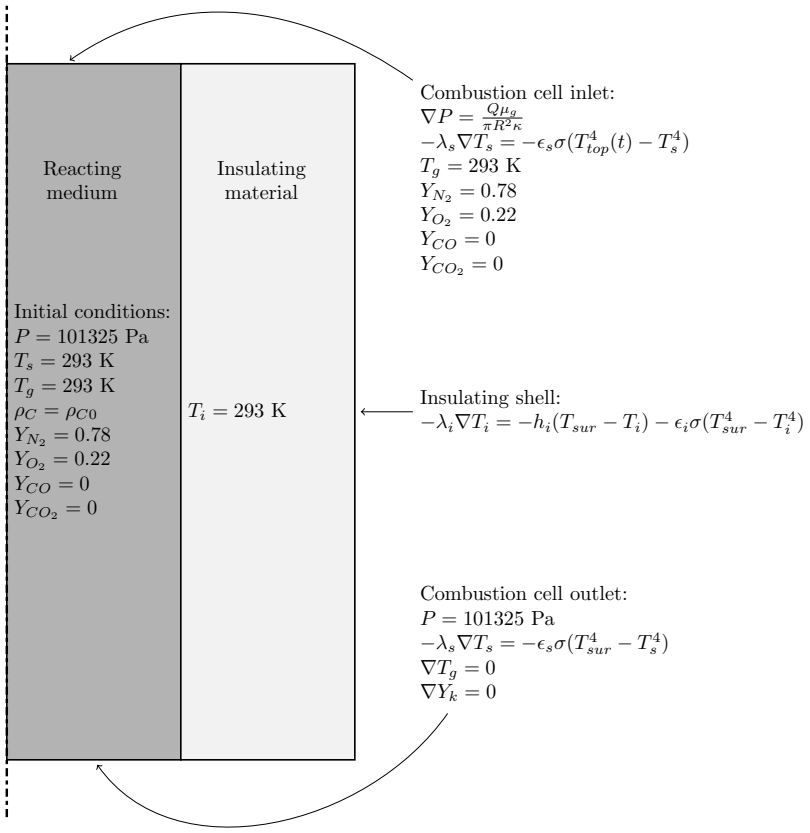

Fig. 2. Numerical domain schematic with boundary conditions

requires local non equilibrium formulation. In order to be as general as possible, we develop such an approach. So, heat balance is governed by 2 equations: one for the solid phase (Eq. 3) and one for the gas phase (Eq. 6). For the solid:

$$\frac{\partial (1-\zeta) \rho_s c_{p_s} T_s}{\partial t} = -\nabla.(-(1-\zeta) \boldsymbol{\lambda_s} \nabla T_s) + HS(T_g - T_s) + \alpha \Pi \omega \quad \textbf{(3)}$$

α is the distribution coefficient for heat source. As explained and demonstrated in (24), this parameter depends on the ratio λ_s/λ_g at the pore scale. Even if the local scale geometry influences this parameter for a high value of this ratio (around 100), most of the heat (*i.e.* 99 %) is distributed to the solid phase. Π is the effective enthalpy depending on the fr_{CO} value. It is calculated as follows:

$$\Pi = (1 - fr_{CO}) \Delta h_{C \mapsto CO_2} + fr_{CO} \Delta h_{C \mapsto CO} \quad \textbf{(4)}$$

with $\Delta h_{C \mapsto CO_2}$ = 32.79 10^6 J/kg, $\Delta h_{C \mapsto CO}$ = 9.210 10^6 J/kg, and ω is the chemical reaction rate expressed as:

$$\omega = A e^{-\frac{Ea}{\Re T_s}} \rho_C Y_{O_2} \quad \textbf{(5)}$$

	Increasing carbon content →						Increasing Péclet number →			
Carbon content (%)	3.6		3.1		2.3		2.3		2.3	
Péclet number	1.6		1.6		1.6		8		16	
	Exp.	Num.	Exp.	Num.	Exp.	Num.	Exp.	Num.	Exp.	Num.
Peak temperature (°C)	1173	1259	1066	1123	709	740	1056	983	1465	1151
Front velocity (mm/min)	5.3	4.5	5.7	4.9	5.2	5.0	17.0	17.4	31.3	33.0
Remaining oxygen (absolute %vol)	0.3	0	0.5	0	5.5	4.3	11.4	9.3	11.3	9.7
fr_{CO} (%vol)	33.2	31.4	25.7	31.4	35.5	31.4	32.1	32.1	23.2	23.2
Air velocity at 20 °C (mm/s)	21	21	21	21	21	21	105	105	210	210
Consumed carbon (%)	100	100	100	100	100	100	100	100	100	100
Front thickness (mm)	4	3	4	4	4	6	8	6	10	7

Table 1. Experimental observations (Exp.) and numerical predictions (Num.)

For the fluid phase:

$$\frac{\partial \zeta \rho_g c_{p_g} T_g}{\partial t} + \rho_g c_{p_g} \nabla.(\vec{v_g} T_g) = -\nabla.(-\zeta \boldsymbol{\lambda_g} \nabla T_g) - HS(T_g - T_s) + (1-\alpha)\Pi\omega \quad \textbf{(6)}$$

In Eq. 3 and 6, $\boldsymbol{\lambda}_s$ and $\boldsymbol{\lambda}_g$ represent the effective conductivities of the two phases, fluid and solid. Their values depend on the local scale properties of each phase and can be estimated using classical weighted average (21), for instance, or through more complex approaches like upscaling procedures (25). According to (25), in non-equilibrium conditions, those properties depend on microstructure, flow and transfers at the local scale. At low thermal Péclet values, a classical conductive regime is observed with constant value of conductivities. However, increasing the Péclet values, we will observe a dispersive regime. The transition between purely conductive and dispersive regimes depend on the microstructure but in (25), when Péclet remains under 10, the dispersive regime could be ignored.

Thermal Péclet number is a ratio between characterisctic times for conduction and heat convection. It is written as follows:

$$Pe_{th} = \frac{(\rho Cp)_g \|\vec{v_g}\| d}{\lambda_g} \quad \textbf{(7)}$$

The thermal Péclet number values range from 2 to 20 for the largest flow rate. However, and according to the results of (25), we will not use dispersive models as only one experimental point exceeds Pe_{th} = 10.

The fr_{CO} parameter was described in the model as follows. The experimental results in (20) reported in Table 1 showed that changing the carbon content did not impact strongly the value of fr_{CO}, and that no clear tendency could be observed. It was decided to keep a constant value of fr_{CO} of 31.4 %vol whatever the carbon content. However, fr_{CO} was observed to vary drastically with air flow variation. The values introduced in the model were 31.4, 32.1 and 23.2 %vol for the air velocities of 21, 105 and 210 mm/s respectively. Thus, fr_{CO} is considered constant throughout the medium and only depends on the flow rate at the inlet.

Several attempts in literature can be found in order to estimate from the local scale structure, the value of the heat transfer coefficient. For instance, one can find an upscaling study leading to an estimate in idealized media (25). Here, we choose to use classical correlations from the literature (26) (Eq. 8).

$$Nu = \frac{4H\zeta}{S\lambda_g} = 0.057\left(\frac{4\rho_g \|\vec{v_g}\|}{S\mu_g}\right)^{0.96} Pr^{1/3} \quad \textbf{(8)}$$

Considering the porous media to be a bed of monodisperse, geometrical considerations lead to the following expression of the specific surface area:

$$S = \frac{6(1-\zeta)}{d} \quad \textbf{(9)}$$

Heat transfer through the insulating shell is described using a classic heat conservation equation:

$$\frac{\partial \rho_i c_{p_i} T_i}{\partial t} = -\nabla.(-\lambda_i \nabla T_i) \qquad \text{in the insulating material} \quad \textbf{(10)}$$

The coupling between the reacting region and the insulating shell is modelled as a perfect contact.We will assume that the heat is transfered from the solid to the insulating shell. It is described by the following set of equations:

$$T_s = T_i \quad \textbf{(11)}$$

on the surface between reacting medium and the insulating material

$$-\lambda_s \nabla T_s = -\lambda_i \nabla T_i \quad \textbf{(12)}$$

on the surface between reacting medium and the insulating material

Finally, the boundary conditions for the insulating material with the ambient conditions are available in figure 2.

3 2. Mass balance in gas phase

Gas flow through the combustion cell was described using continuity combined with ideal gas assumption and Darcy's law in a similar way to (15) or (27).

$$\frac{\partial \zeta \rho_g}{\partial t} + \nabla.(\rho_g \vec{v_g}) = \sum_{i,g} \omega_{i,g} \quad \textbf{(13)}$$

The gas is assumed to behave as an ideal gas, thus its density can be expressed as:

$$\rho_g = \frac{PM_g}{\Re T_g} \quad (14)$$

Combining Eq. 13 and 14, we obtain Eq. 15:

$$\frac{\partial \frac{\zeta M_g}{\Re T_g} P}{\partial t} + \nabla.(\rho_g \vec{v_g}) = (1 - fr_{CO})\omega \frac{M_{CO_2} - M_{O_2}}{M_C} + fr_{CO}\omega \frac{M_{CO} - M_{O_2}}{2M_C} \quad (15)$$

In our case, pore Reynolds number varies from 1 to 30, depending on the flow rate. According to the general Forchheimer equation we have:

$$\nabla P = \frac{\mu}{\kappa}\vec{v_g} + \frac{\rho F}{\mu\sqrt{\kappa}}\|\vec{v_g}\|\vec{v_g} \quad (16)$$

where F is the Forschheimer coefficient accounting for inertial terms at the local scale from drag (28).

In a recent experimental study (29), the Forchheimer coefficients were obtained for various media. For spheres packing, with diameter ranging from 1 to 3 mm, F ranges between 0.43 (3 mm) to 0.54 (1 mm). Another way is to chose a unique formulation of κ depending on the Reynolds number values. According to (30) and in agreement with the work of (31) and (32), κ in the main flow direction can be correlated, for intermediate Re values, lesser than some hundreds, using:

$$\kappa^* = \frac{\kappa}{1 + \gamma\sqrt{Re_p}} \quad (17)$$

According to (32), γ value is around 0.30 for structured packing and in the case of (29), this varies from 0.11 to 0.14 for respectively 1 and 3 mm spheres packings. It is then possible to use:

$$\vec{v_g} = -\frac{\kappa^*}{\mu_g}\nabla(P - \rho_g\vec{g}) \quad (18)$$

Then, combining Eq. 15 and 18, we obtain Eq. 19:

$$\frac{\partial \frac{\zeta M_g}{\Re T_g} P}{\partial t} - \nabla.(\rho_g \frac{\kappa^*}{\zeta\mu_g}\nabla(P - \rho_g\vec{g})) = (1 - fr_{CO})\omega \frac{M_{CO_2} - M_{O_2}}{M_C} + fr_{CO}\omega \frac{M_{CO} - M_{O_2}}{2M_C} \quad (19)$$

As densities and viscosities vary in space, we will obtain a non uniform field of permeability, depending on the flow regime imposed by the mass flux, but also by local thermodynamic conditions.

3 3. Mass balance in solid phase

Solid carbon residue is immobile, and a classical balance equation with reaction is used:

$$\frac{\partial(1-\zeta)\rho_C}{\partial t} = -\omega \quad (20)$$

At the macro scale, transport of the gaseous species is classically represented by a convection/dispersion equation:

$$\frac{\zeta\rho_g\partial Y_k}{\partial t} + \nabla.(\rho_g\vec{v_g}Y_k) = \nabla.(\zeta\rho_g\overline{\overline{\boldsymbol{D_k^*}}}\nabla Y_k) + \omega_k \quad (21)$$

With:

$$\omega_{O_2} = (1 - fr_{CO})\omega\frac{M_{O_2}}{M_C} - fr_{CO}\omega\frac{M_{O_2}}{2M_C} \quad (22)$$

$$\omega_{CO_2} = (1 - fr_{CO})\omega\frac{M_{CO_2}}{M_C} \quad (23)$$

$$\omega_{CO} = fr_{CO}\omega\frac{M_{CO}}{M_C} \quad (24)$$

$\overline{\overline{\boldsymbol{D_k^*}}}$ is a second order tensor expressed usually like:

$$\overline{\overline{\boldsymbol{D_k^*}}} = \begin{pmatrix} D_T^* & 0 & 0 \\ 0 & D_T^* & 0 \\ 0 & 0 & D_L^* \end{pmatrix} \quad (25)$$

where D_L^* is the longitudinal dispersion and D_T^* the transverse dispersion coefficient. In this study, we will use classical dependence of those coefficients with the flow velocity assuming linear dispersive regime (25). We will ignore extra diagonal terms. There are classically lower than the diagonal terms up to 2 orders of magnitude (25).

$$D_L^* = \beta_L\|\vec{v_g}\| + D^* \quad (26)$$

$$D_T^* = \beta_T\|\vec{v_g}\| + D^* \quad (27)$$

Respectively, β_L and β_T are the longitudinal and transverse dipersivities.

D^* is the effective diffusion coefficient accounting for the slow down of diffusion due to the microstructure of the porous medium. According to (25), in the purely diffusive case, we obtain:

$$D^* = \frac{D}{\tau} \quad (28)$$

with a tortuosity τ fo 1.14 (33)

Moreover, when dispersive regimes are linear, we obtain:

$$D_k^* = D^* I + \|\vec{v_g}\|(\beta_L\frac{\vec{v_k}X\vec{v_g}}{\|\vec{v_g}\|^2} + \beta_T\frac{\vec{v_k}X\vec{v_g}}{\|\vec{v_g}\|^2}) \quad (29)$$

with $\beta_L = d$ and $\beta_T = d/10$

Nitrogen is the diluent specie, so we impose the following constraint:

$$Y_{N_2} = 1 - Y_{O_2} - Y_{CO} - Y_{CO_2} \quad (30)$$

3 4. Physical properties

Physical properties are available in Tables 2 and 3. Because of the wide range of temperature that the model has to cover,

the evolutions with temperature of several physical properties had to be taken into account (solid and gas thermal conductivities, solid and gas heat capacities, gas diffusivity and gas viscosity). Correlations coming from literature or from manufacturer's data were used to describe physical property variations (alumina thermal capacity (34), insulating material - manufacturer's data - (35)) (36). Radiation inside of the porous bed was taken into account using Rossland model (Eq. 31) (36).

The gas phase is a mixture of nitrogen, oxygen, carbon monoxide and carbon dioxide. As air is used to feed the combustion process, nitrogen content remains high throughout the combustion cell. Thus, nitrogen was taken as model gas to evaluate gas phase physical properties (thermal capacity (34), thermal conductivity (37), dynamic viscosity (38)).

$$\lambda_s = \lambda_{Al_2O_3} + \frac{16}{3}\zeta d\sigma T_s^3 \qquad \textbf{(31)}$$

4. Equation system solving and kinetic parameters fitting

The equation system was solved using implicit sequential algorithms provided by the open source solver OpenFOAM. We use a sequential approach, solving step by step all the equations. We use an implicit formulation, and we use a second order numerical scheme. The mesh convergence was achieved using a 60000 square cells mesh. The runtime is about 35h to produce 2h30 of physical time on a single thread [1]. The kinetic parameters for the carbon oxidation reaction A and Ea where the only parameters adjusted in the model. Their value was determined to obtain the best fitting between the model predictions and all of the experimental cases considered in the work. To do so, we used 3 indicators along the cell axis were compared to experimental observations: the front temperature, the front velocity and O_2 concentration remaining in the flue gas. To perform this optimisation process based on multi-objective analysis, we could use the same approach as in (39). However, this requires to define an objective function and then to determine the best parameters fitted to minimize the errors. This is a dedicated study, and it is not the scope of this paper.

Rather, a screen was conducted in order to fit the kinetic parameters for the carbon oxidation reaction A and Ea. The starting point was the kinetic parameters proposed in (20): A =0.327 1/s and Ea = 18500 J/mol. Yet, they yielded poor results. It is known from literature that parameters, even carefully measured, in TG experiments may have to be significantly changed in order to yield proper results in bed model (40). Figure 4 reports the screening results. From this figure, one can see that two main areas emerge: a combustion extinguishment zone (for a given Ea, when A is too low) and a complete O_2 consumption zone (for a given Ea, when A is too high). The transition zone in between these two zones was investigated to find the best fitting values. In the end, the couple A = 400 1/s and Ea = 55500 J/mol yielded the best results. Figure 3 shows that with the best fitting parameters a

[1] Intel Core i7-4910 MQ Haswell at 2.90 MHz, 8 Go DDR3 1600 MHz

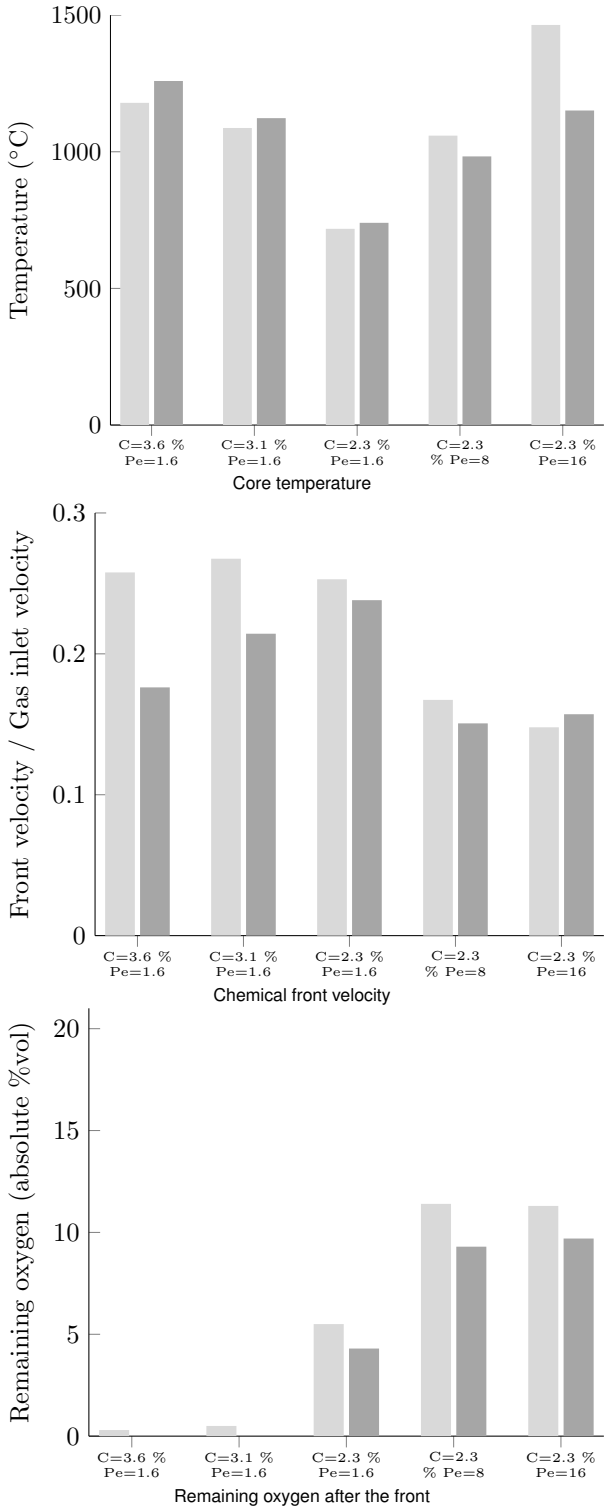

Fig. 3. Experimental observation and numerical predictions. Light gray: experimental observations, dark gray: numerical predictions

prediction of the three main front characteristics is obtained over the large ranges of experimental parameters. Significant discrepancies can be observed in some cases, but it is judged that they remain acceptable considering the complexity of the smouldering process and the quite simple description adopted in the model. It is stated, at this stage, that the main objective of the work is reached here: it is possible to describe

Symbol	Name	Value	Dimension	Reference
$\lambda_{Al_2O_3}$	Alumina thermal conductivity	0.447	W/m/K	Measured
ρ_s	Sphere density	1475	kg/m^3	Measured
ζ	Porosity	0.452	-	Measured
κ	Permeability	2.809 10^{-9}	m^2	Estimated with Kozeny Carman law
τ	Tortuosity	1.14	-	(33)
S	Specific surface area	1644	1/m	Estimated
d	Average sphere diameter	2 10^{-3}	m	Measured
R	Reacting medium diameter	91 10^{-3}	m	Measured
ϵ_s	Emissivity	0.5	-	Estimated
T_{sur}	Surrounding temperature	293	K	Measured

Table 2. Reacting medium physical properties

Symbol	Name	Value	Dimension	Reference
ρ_i	Density	673	kg/m^3	Measured
h_i	Convective heat transfer coefficient	10	W/m^2/K	Estimated as free convection
ϵ_i	Emissivity	0.1	-	Estimated

Table 3. Insulating material physical properties

the main characteristics of a smouldering front – including cases where not all of the oxygen is consumed – with a simplified description concerning the chemical reaction. We remind here that the fr_{CO} had to be given to the model; this remains the main weak point of the model.

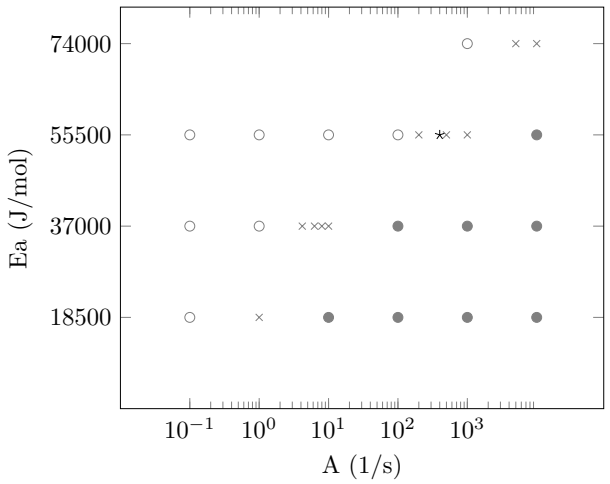

Fig. 4. Screening for A and Ea. Open circle: combustion extinction, closed circle: complete oxygen consumption, cross: potential values, star: best fitting values

It is interesting here to compare the identified values of A and Ea to those determined by (20) in thermo-gravimetric experiments. These parameters were derived from isolated particles situation in controlled temperature and oxygen surrounding. The measured activation energy was 18500 J/mol, which is approximately 3 times smaller than the value identified in the model in bed configuration. It is difficult to interpret quantitatively this difference. It can nevertheless be concluded that the simple approach consisting in measuring the kinetic parameters on a single particle and injecting them in a bed scale model is not satisfactory. We use a constant activation energy like in (41) who showed that a constant activation energy for carbon oxidation is observed if temperature does not exceed 1650 K.

In the following section, we will focus our analysis on the coupled phenomena governing the front characteristics and discuss some results by comparison with available experimental data.

5. Inputs of the model for comprehension of coupled phenomena

5 1. Temperature field

Firstly, we use a set of conditions in order to establish the ability of our numerical model to capture all the physical phenomena taken into account. We will compare some experimental data to the ones of the numerical model:

- the front temperature and width along the axis of the cell at 20 cm from the inlet
- radial temperatures, to see if we capture the heat losses
- temperature signal at the surface of the insulating shell

Despite the quite large diameter of the combustion cell used in the experiments, compared to other works in literature, heat losses at the cell walls have a strong impact. For instance, the computed temperature field after 1 h is presented in figures 5 and 6 for the reference case, with 2.30 %C and 21 mm/s air velocity in the reactive bed, and in the insulating shell. The temperature level reaches a maximum on the axis (741°C) then radially decreases to 323°C at the inner surface of the cell. The transverse profiles exhibit the same information more quantitatively (Fig. 6).

Figure 7 reports the temperature history of one thermocouple at the axis of the reacting medium. The experimentally reported history exhibits at first a plateau around 60 °C, which is attributed to water vaporization and condensation (14). Then, temperature rises until a peak value of 709 °C is reached. Afterwards, temperature decreases slowly. The

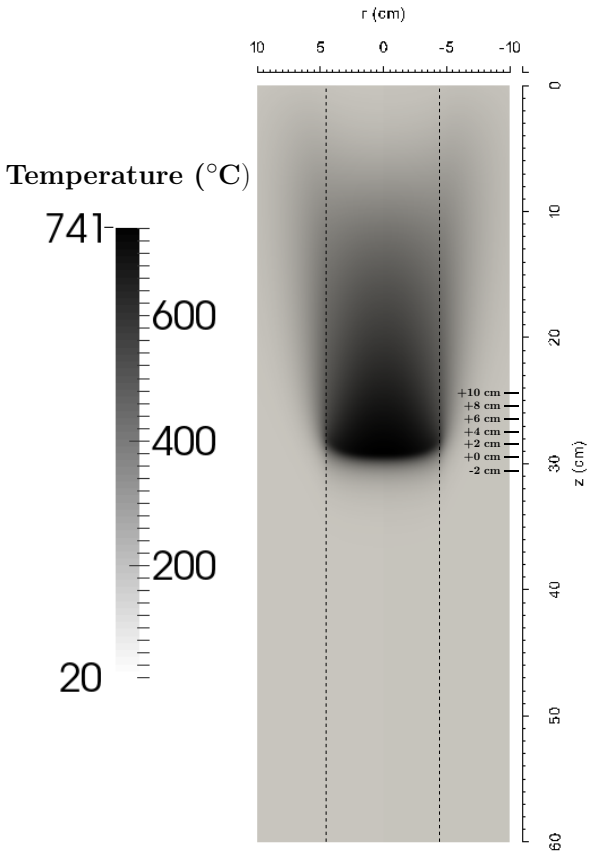

Fig. 5. Solid temperature field inside of the combustion cell after 1 h. C = 2.3 %, Pe = 1.6. Locations marked: position relative to the chemical front (as used in Fig. 6)

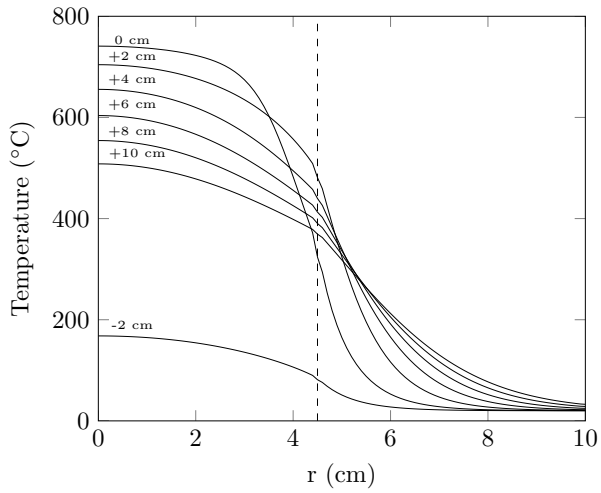

Fig. 6. Solid temperature profiles after 1 h at various locations relative to the front (Fig. 5). Front position: 29 cm. C = 2.3 %, Pe = 1.6

numerical model provides temperature for both solid and gas phase. These two temperature histories are quite close. It can be explained by the high value of the solid gas convective heat transfer coefficient (H). Yet, gas temperature increases a few moments before solid temperature. This is due to the fact that the gas heats up in contact with the reacting solid, before being pushed forward into the cell. Then, in turn, the gas heats up the solid downstream the front which later allows its ignition. This is how the combustion front propagates into the medium. From now on, only solid temperature will be considered. Numerically computed temperature history - in which the water vaporization and condensation was not taken into account - shows the same trend as the experimental one. The model predicts a peak temperature of 741 °C, which is very close to monitored temperature. Agreement between numerical prediction and experimental observations appears then to be very good.

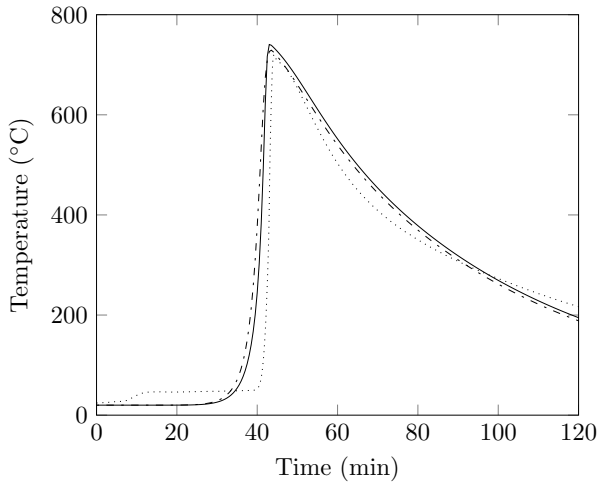

Fig. 7. Temperature history on the revolution axis at 19 cm from the inlet. Continuous line: model solid temperature, dashed line: model gas temperature, model, dotted line: experimental observations. C = 2.3 %, Pe = 1.6

Figure 7 reports the temperature history of one thermocouple at the axis of the reacting medium. The experimentally reported history exhibits at first a plateau around 60 °C, which is attributed to water vaporization and condensation (14). Then, temperature rises until a peak value of 709 °C is reached. Afterwards, temperature decreases slowly. Numerically computed temperature history - in which the water vaporization and condensation was not taken into account - shows the same trend as the experimental one. The model predicts a peak temperature of 741 °C, which is very close to monitored temperature. Agreement between numerical prediction and experimental observations appears then to be very good.

In order to check the accuracy of the 2D model, the experimental history of the thermocouples placed 1 cm away from the walls inside the reactive medium is reported in figure 8, together with the model predicted evolution. Experimental observation reports several temperature histories for those thermocouples. Indeed, in the experiments the front can be tilted with respect to the horizontal. Therefore, temperature histories vary according to the angular positions. Once again, a good agreement is obtained. After 40 minutes, a rapid exponential increase of temperature is observed to reach 650 °C in several minutes. Then, a slow exponential cooling appears. Values of decay length are given in (20) depending of the Péclet values. We do not reach the expected level of temperatures with a difference close to 100 °C for the worst cases. Anyway, the trends are well captured. Part of the discrepancy can be explained by uncertainties in the insulating heat capacity whose maximum values of the temperature are de-

pendent on. Perfect boundary conditions could also be questionable. We must also keep in mind that fr_{CO} is a constant in our case. A small variation of the value could lead to large increase in temperature levels, when favouring CO_2 formation. This requires the determination of a complex model for fr_{CO}, depending from temperature level for instance. As we focus on determining the principal phenomena involved in the evolution of front shape, we will make the use of this simplified approach.

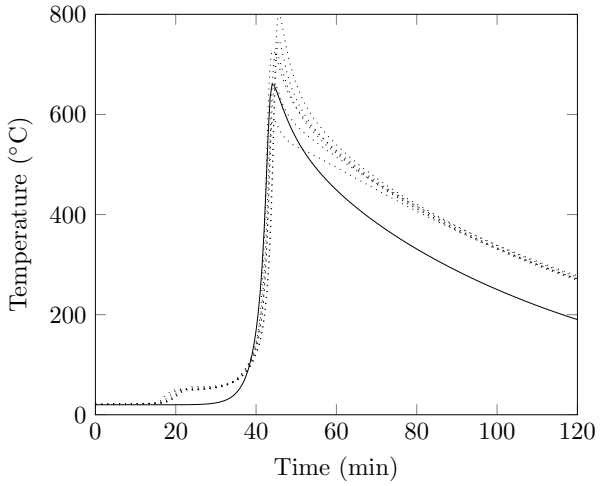

Fig. 8. Solid temperature history 1 cm away from the wall at 19 cm from the inlet. Continuous line: model, dotted line: experimental observations. C = 2.3 %, Pe = 1.6

Capturing the temperature profile of the outer surface of the cell is a token of the quality of the heat loss through the insulating layer modelling. Both experimental observations and numerical predictions are reported in figure 9. As one can see, the numerical model is able to reproduce the trends of the outer surface temperature history. The predicted outer surface temperature peak is very close to the monitored one: 55 °C for 60 °C. Thus, we can estimate that our model reproduces fairly well the thermal transport in a complex situation with multi-layered media, heterogeneous in terms of properties.

Based upon this, the model can be used to estimate the amount of energy lost at the walls, compared to the heat released at carbon oxidation. The heat losses at the cell walls were estimated by integrating the heat flux over time, all along the cell. The heat released by carbon combustion can be calculated from the mass of carbon in the cell and the reaction heat calculated from Eq. 4. In the reference case Pe = 1.6, C = 2.3 %, approximately 50 % of the combustion energy is lost through the cell walls. This confirms the necessity of insulating the combustion cell. Even for this quite high diameter cell - as compared to other experimental devices used in the literature - half the energy released is lost and not left in the gas to flow downstream.

As reported in Table 1, the agreement between the model predictions and the experimental observations, in terms of temperature at the center of the cell, is good for all the cases, except the highest Péclet number. The discrepancy is thought to come from the fr_{CO} values used in the model which are

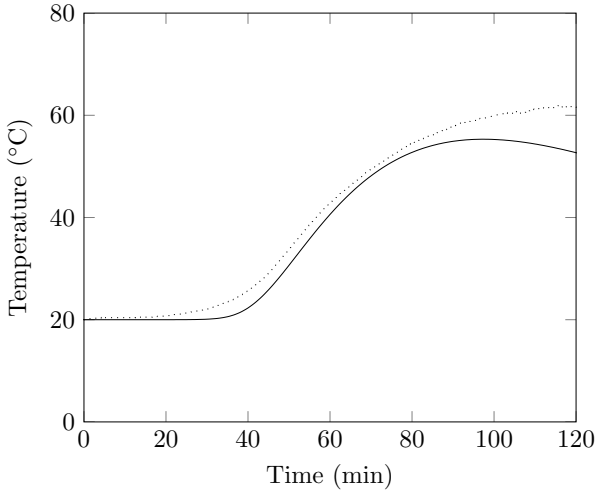

Fig. 9. Superimposition of the solid temperature histories on outer surface of the cell at 19 cm from the inlet. Continuous line: model, dotted line: experimental observations

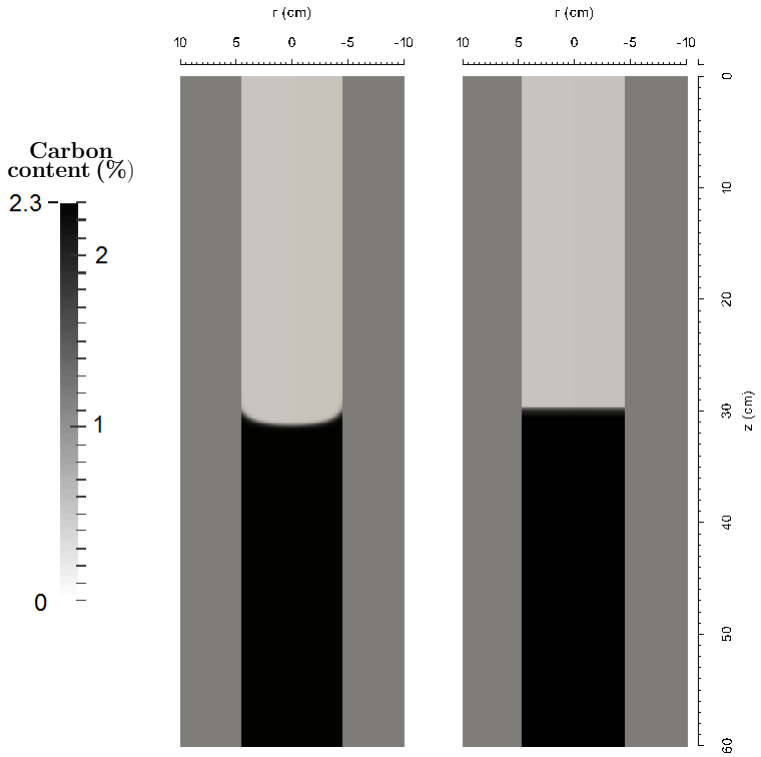

Fig. 10. Carbon field inside of the combustion cell when half of the medium has been consumed. On the left: with heat loss, on the right: without the heat loss. Color legend: the darker, the higher

constant over the medium. fr_{CO} has indeed a strong impact on the heat released by the oxidation reaction and therefore on the temperature. Discrepancies for the highest Péclet number case may come also from the fact that thermal dispersive effects were not taken into account. In this particular case, Péclet number value suggested that these effects may play a role on thermal behaviour of the medium. Anyway and as a partial conclusion, our aim was to check if our model was able to capture most of the effects involved in the combustion front propagation. We could assume that our model is really

close to the experimental reference and we could now explore make the use of it to study the deformation of the front due to heat losses.

5 2. Carbon field and front shape

In order to allow for a general observation of the impact of heat loss on the front shape, a numerical experiment was carried out. Two simulations were run, one this the heat loss enabled the other with the heat loss disabled. Figure 10 reports the results of this experiment in term of carbon density field. When heat loss are taken into account, the front shape exhibits a curvature. This curvature is not present when heat loss are missing. From this numerical observation, it can be concluded that heat loss are the source of the front shape curvature.

Using the model, we focus on 3 configurations to determine the shapes of the smouldering front. Figure 11 reports the modelled shapes of the smoldering front in three extreme configurations. For the reference case (placed at the center) a downward curved front is observed after 10 cm, and is preserved during front propagation as illustrated at z = 20 cm. The observation is similar with high air flow rate. In the case of high carbon content (left), the front is strongly curved upward; the phenomenon accentuates with the propagation. To support the interpretation of these results, figure 12 reports the amount of oxygen left in the gas downstream of the front. It can be seen that the situation can shift from total consumption of oxygen to more than half the fed oxygen percolating through the front. During the experiments reported by (20), such curved shapes of the fronts were observed. The curvature was sometimes upward and sometimes downward, even for fixed experimental condition such as the reference case. Understanding why a front is not flat is interesting for a man-controlled applications because it underlies the front stability question. There are several reasons to explain the front shape change as already discussed in (42). The front velocity is basically controlled by the chemical reaction stoichiometry.

As long as all of the carbon is consumed and all of the fed O_2 used, the local front velocity is governed by the local axial oxygen flow rate. The local temperature can impact this flow rate in several ways. If the temperature is lower (as observed closed to the cell walls) the gas density is higher and the front is faster. A low temperature also induces a smaller gas viscosity, favouring high local gas velocity and a faster front propagation.

If not all of the oxygen is consumed at the front, the front will slow down. This is likely to occur if the local temperature is low. If not all of the carbon is oxidized, the front will accelerate.

Sphere packings near the walls is not homogeneous as it is in the bulk of the bed; then permeability is locally increased (43). This may lead to an increased gas flow rate and to a local front acceleration.

In the following, it is shown that the developed model can bring valuable understanding of the coupled phenomena governing the front shape evolution.

In the reference case and the high air velocity cases, the front shape is stable. This means that the different phenomena that operate to accelerate and to slow down the front at the walls are balanced. The front shape in the high carbon content experiment is not stable: the front is faster at the walls. The potential phenomenon to slow down the front is the percolation of oxygen at the walls. Indeed, 3.5 % oxygen is

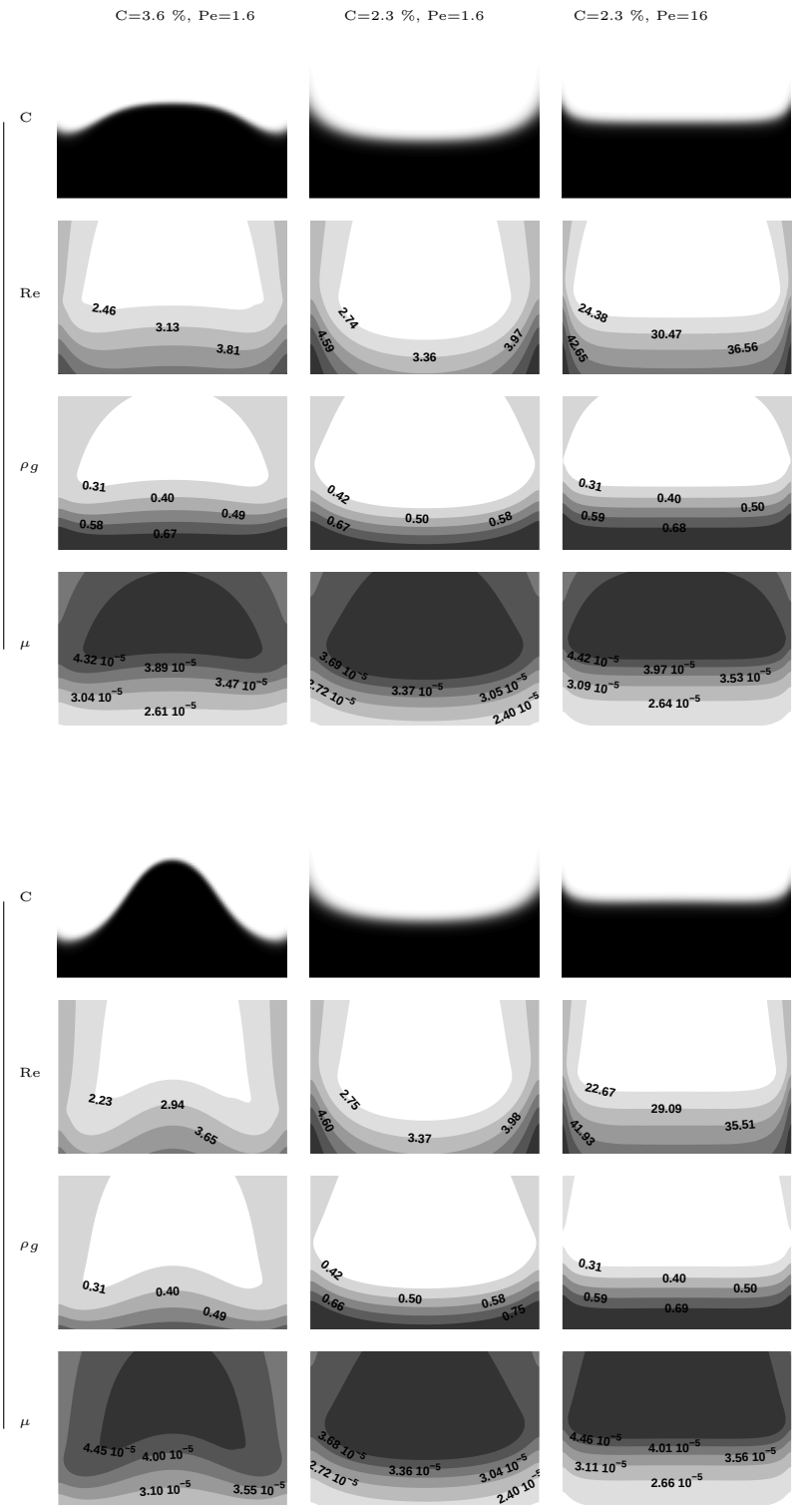

Fig. 11. Different fronts shapes, viscosity, density and Reynolds number maps observed in the reference case (center), with high carbon content (left) and with high gas velocity (right). Color legend: the darker, the higher

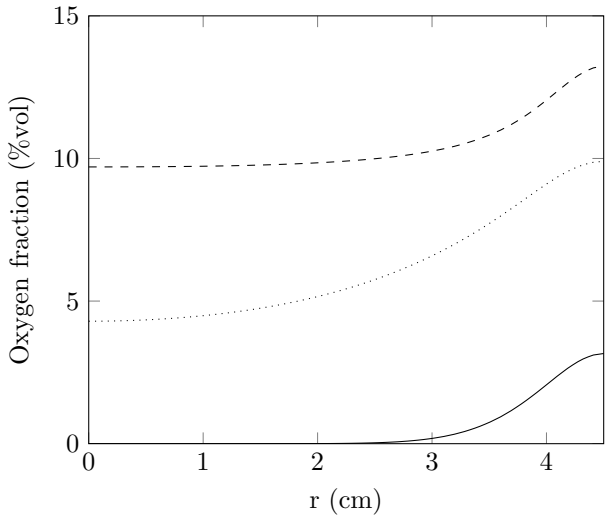

Fig. 12. Remaining oxygen downstream of the front. Continuous line: C = 3.6%, Pe = 1.6, dotted line (reference case): C = 2.3%, Pe = 1.6, dashed line: C = 2.3%, Pe = 16

predicted by the model at the walls downstream of the front, while no oxygen percolated at the cell axis. This plays a minor role as compared to front accelerating phenomena, i.e. colder temperature of the gases at the walls. It implies that:

- density and oxygen concentrations are higher at the walls
- the gas viscosity is smaller and the local gas velocity is higher

The numerical model was used to estimate the contribution of the two phenomena. This remains an indication of the possible effects of both density and viscosity on the front shape. But, in the past, this was mentioned in (15), as well as channelling effects. Even if we show exhibit that heat losses is the main phenomenon explaining front curvature, they generate on the fluid properties two important effects:

- higher density at the walls, responsible for three quarters of the front deformation
- smaller gas viscosity and higher local gas velocity, responsible for one quarter of the deformation

The proportion of the importance was obtained by inhibiting turn by turn density variation at first and then, viscosity variation.

The sphere arrangement also may explain part of the faster propagation of the front at the walls. Nevertheless, the porosity increase was reported to be in a ratio of about 2 but only in a 1 particle thick zone at the walls (43). We believe that this effect was negligible. Hence, it was not implemented in the model.

Furthermore, the curved shape of the front in high carbon content cases may explain the discrepancies between experimentally reported front velocities at the center of the cell and numerically predicted ones (Table 1). Indeed, the numerical model over predicts the propagation of the combustion front near the wall for these cases, meaning that oxygen is diverted towards the cell walls. It leads to a lower oxygen flow rate at the center of the cell and therefore a lower front velocity at this location. One of the important results here is the determination of this front velocity. Using the signal obtained thanks to thermocouples, combustion front velocity could lead to a bad estimate in the case where the front is curved. We will take, at the axis, the maximum of the recorded temperatures, and then use classically this as a reference for the front location. In this study, we clearly demonstrate that this curvature is important and increases with time depending on several parameters. Determining the real front location is then subject to discussion but in Table 1, we report not the maximum of the temperatures at the axis but the location of the points, in the longitudinal direction, where 50 % of the carbon is consumed. The stoichiometry of carbon consumption by the fed oxygen has been expressed in Eq. 2 by (42).

It gives the theoretical front velocity as a function of the experimental parameters. According to (20), these values range from 5 (Pe = 1.6), 19mm/min (Pe = 8) to 36.5 mm/min (Pe = 16) when carbon content is fixed at 2.3 %. The values in Table 1, for the last three cases, refer to these points. Then, one could see that our numerical model is close to the observed front temperature but also close to the theoretical ones.

5 3. Front thickness

In order to check the accuracy of our approach, we have one last indicator. This is the front thickness, depending on flow regime (Péclet number) but also on carbon content (values of temperature). It has been investigated in detail by (14). The front structure was explained and the thickness of reactive zone reported using gas microsampling.

We quantify this as the distance between the positions where carbon conversion shifts from 10 % to 90 %. Table 1 reports the experimentally observed thickness's in (20) and the model predicted ones. The present model appears to predict thickness's comparable to experimental ones, which can vary between 2 and 5 average particle diameters. The model also recovers the increase of the front thickness when air velocity increases. This will be taken here just as a remark, and no particular signification will be attributed to this result. Since the kinetic parameters of the carbon oxidation reaction were fitted, it is not totally surprising that the description of the front thickness has a good order of magnitude. The quite good description of a very complex pore scale problem by the present Darcy scale model may be accidental to some extent.

6. Conclusion

In this study, we develop a fully coupled heat and mass transport model in order to investigate the effects of different phenomena involved when dealing with combustion in porous media. We use a 2D Darcy scale model with a complete description of the whole phenomenology while taking into account heat losses around the reacting medium. We use a simplified chemical model based on a single oxidation reaction and a constant value of fr_{CO}. We determine the kinetic

parameters by minimizing the error between a set of experiments and the model predictions. The model predictions are satisfying in terms of front temperature, front velocity, and non-consumed oxygen amount over a variety of situations - with different carbon contents and air velocities, including cases in which some oxygen percolates through the front. This clearly demonstrates the ability of this tool to capture the main features of the smoldering process. The remaining discrepancie were mainly attributed to the two weaknesses of the model: a constant fr_{CO} over the domain, and a very simplified description of the chemical reaction.

The model was used to bring new understanding of the effect of the heat loss on the front shape. The local cooling at the walls induces a higher gas density which is the phenomenon controlling the local front shape, with only a minor contribution from the lower gas viscosity. It also enables to quantify the heat loss at the walls that are as high as half of the energy released at carbon oxidation. Accurate description of this loss is necessary to model high temperature smouldering experiments, even in a combustion cell with a diameter as high as 91 mm.

In this work, a very simplified description of the chemical reaction was used, but it required taking the fraction of carbon oxidized into CO from experiments. In future works, it might be envisioned to prescribe the value of fr_{CO} as a function of local thermodynamic conditions, i.e. gas velocity and temperature level.

Acknowledgement

The authors would like to thank the French *Agence Nationale de la Recherche* for financial support of the INSICOMB project ANR-11-BS009-005-01 in which this work was carried on. We would like to thank Bernard Auduc and Denis Marty for their technical support.

References

1. I. Yucel Akkutlu and Yanis C. Yortsos. The dynamics of in-situ combustion fronts in porous media. *Combustion and Flame*, 134(3):229–247, August 2003. ISSN 0010-2180. .
2. A. A. Mailybaev, J. Bruining, and D. Marchesin. Analysis of in situ combustion of oil with pyrolysis and vaporization. *Combustion and Flame*, 158(6):1097–1108, June 2011. ISSN 0010-2180. .
3. Jean-Pierre Vantelon, Bénigne Lodeho, Stephane Pignoux, Janet L. Ellzey, and José L. Torero. Experimental observations on the thermal degradation of a porous bed of tires. *Proceedings of the Combustion Institute*, 30(2):2239–2246, January 2005. ISSN 1540-7489. .
4. Paolo Pironi, Christine Switzer, Guillermo Rein, Andres Fuentes, Jason I. Gerhard, and Jose L. Torero. Small-scale forward smouldering experiments for remediation of coal tar in inert media. *Proceedings of the Combustion Institute*, 32(2):1957–1964, 2009. ISSN 1540-7489. .
5. Guillermo Rein, Natalie Cleaver, Clare Ashton, Paolo Pironi, and José L. Torero. The severity of smouldering peat fires and damage to the forest soil. *CATENA*, 74(3):304–309, August 2008. ISSN 0341-8162. .
6. Susan E. Page, Florian Siegert, John O. Rieley, Hans-Dieter V. Boehm, Adi Jaya, and Suwido Limin. The amount of carbon released from peat and forest fires in Indonesia during 1997. *Nature*, 420(6911):61–65, November 2002. ISSN 0028-0836. .
7. M Sennoune, S Salvador, and G Debenest. Impact of a co2-enriched gas on the decarbonation of caco3 and the oxidation of carbon in the smoldering process of oil shale semicoke. *Energy & Fuels*, 26(1):391–399, 2011.
8. A. P. Aldushin, B. S. Seplyarskii, and K. G. Shkadinskii. Theory of filtrational combustion. *Combustion, Explosion and Shock Waves*, 16(1):33–40, January 1980. ISSN 0010-5082, 1573-8345. .
9. Da Schult, Bj Matkowsky, Va Volpert, and Ac Fernandezpello. Propagation and Extinction of Forced Opposed Flow Smolder Waves. *Combustion and Flame*, 101(4):471–490, June 1995. ISSN 0010-2180. . WOS:A1995RA12600008.
10. D. A. Schult, A. Bayliss, and B. J. Matkowsky. Traveling waves in natural counterflow filtration combustion and their stability. *Siam Journal on Applied Mathematics*, 58(3):806–852, June 1998. ISSN 0036-1399. WOS:000072695600006.
11. C. Yang and G. Debenest. Numerical Simulations for Smoldering in a Horizontal Channel: Comparisons Between Variable Density-Based Formulation and Incompressible One. *Combustion Science and Technology*, 186(12):1954–1974, December 2014. ISSN 0010-2202. .
12. G. Debenest, V. V. Mourzenko, and J. F. Thovert. Smouldering in fixed beds of oil shale grains: governing parameters and global regimes. *Combustion Theory and Modelling*, 9(2): 301–321, May 2005. ISSN 1364-7830. .
13. Mustafa Elayeb. *Modélisation à l'échelle microscopique de transports avec réaction en milieu poreux: combustion en lit fixe*. 2008.
14. M. F. Martins, S. Salvador, J.-F. Thovert, and G. Debenest. Co-current combustion of oil shale - Part 2: Structure of the combustion front. *Fuel*, 89(1):133–143, January 2010. ISSN 0016-2361. . WOS:000271295000017.
15. Hossein Fadaei, Mohammed Sennoune, Sylvain Salvador, Alexandre Lapene, and Gerald Debenest. Modelling of non-consolidated oil shale semi-coke forward combustion: Influence of carbon and calcium carbonate contents. *Fuel*, 95(1):197–205, May 2012. ISSN 0016-2361. . WOS:000300615900026.
16. R. Zajdlik, L. Jelemensky, B. Remiarova, and J. Markos. Experimental and modelling inves-

Latin symbols

A	pre exponential factor	1/s
c_p	screen specific heat capacity	J/kg/K
C	carbon mass fraction in the solid phase	-
D	mass diffusion coefficient	m^2/s
$\boldsymbol{D}$	effective mass diffusion coefficient	m^2/s
d	sphere diameter	m
Ea	activation energy	J/mol
fr_{CO}	carbon monoxide fraction	-
fr_{Coxi}	fraction of carbon oxidized by the combustion front	-
fr_{Ooxi}	fraction of oxygen consumed by the combustion front	-
$\vec{g}$	acceleration due to gravity	m/s^2
H	solid gas convective heat transfer coefficient	$W/m^2/K$
h	convective heat transfer coefficient	$W/m^2/K$
M	molar mass	g/mol
Nu	Nusselt number	-
P	pressure	Pa
Pe	Péclet number	-
Pr	Prandtl number	-
Q	volumic flow rate	m^3/s
$\Re$	ideal gas constant	J/mol/K
R	reacting medium radius	m
Re	Reynolds number	-
S	porous medium specific surface area	1/m
T	average macroscale temperature	K
t	time	s
$\vec{v}$	velocity	m/s
Y	mass fraction	-

Greek symbols

α	distribution coefficient for heat source	-
β	dispersiviity	m
Δh	latent heat	J/kg
ϵ	emissivity	-
ω	reaction rate	$kg/m^3/s$
λ	thermal conductivity	W/m/K
$\boldsymbol{\lambda}$	effective thermal conductivity	W/m/K
κ	permeability	m^2
ρ	density	kg/m^3
σ	Stefan-Boltzmann constant	$W/m^2/K^4$
Π	reaction heat	W/m^3
μ	dynamic viscosity	Pa.s
τ	tortuosity	-
ζ	porous media porosity	-

Subscripts

Al_2O_3	alumina
bed	bed
frc	chemical front
g	gas phase
i	insulating material
k	accounting for the different gaseous species (N_2, O_2, CO and CO_2)
L	longitudinal
p	pore
s	solid phase
sur	surrounding
T	transverse
th	thermal
top	top of the combustion cell

Other symbols

$\overline{\overline{A}}$	tensors
$\|\vec{a}\|$	vector $\vec{a}$ norm
∇	nabla operator

Table 4. Nomenclature

tigations of single coal particle combustion. *Chemical Engineering Science*, 56(4):1355–1361, February 2001. ISSN 0009-2509. . WOS:000167819200017.

17. Chen Yang, Jean-François Thovert, and Gérald Debenest. Upscaling of mass and thermal transports in porous media with heterogeneous combustion reactions. *International Journal of Heat and Mass Transfer*, 84:862–875, May 2015. ISSN 0017-9310. .
18. Mehdi Maerefat, M. Khosravy El-Hossaini, and K. Mazaheri. Numerical modeling of two-dimensional cylindrical porous radiant burners with sidewall heat losses. *Journal of Porous Media*, 14(4), 2011.
19. Tanzeer Hasan, Jason I. Gerhard, Rory Hadden, and Guillermo Rein. Self-sustaining smouldering combustion of coal tar for the remediation of contaminated sand: Two-dimensional experiments and computational simulations. *Fuel*, 150:288–297, June 2015. ISSN 0016-2361. .
20. Sylvain Salvador Germain Baud. New Granular Model Medium To Investigate Smoldering Fronts Propagation—Experiments. *Energy & Fuels*, 29(10), 2015. ISSN 0887-0624. .
21. Ej Kansa, He Perlee, and Rf Chaiken. Mathematical-Model of Wood Pyrolysis Including Internal Forced-Convection. *Combustion and Flame*, 29(3):311–324, 1977. ISSN 0010-2180. . WOS:A1977DU60400010.
22. G. Debenest, V. V. Mourzenko, and J.-F. Thovert. Three-Dimensional Microscale Numerical Simulation of Smoldering Process. *Combustion Science and Technology*, 180(12):2170–2185, 2008. ISSN 0010-2202. . WOS:000260228100005.
23. A. A. M Oliveira and M Kaviany. Nonequilibrium in the transport of heat and reactants in combustion in porous media. *Progress in Energy and Combustion Science*, 27(5):523–545, 2001. ISSN 0360-1285. .
24. Bruno Ladevie Michel Quintard. Effect of homogeneous and heterogeneous source terms on the macroscopic description of heat transfer in porous media. *Symposium on Energy Engineering in the 21st Century, Begell House, New York*, 2:482–489, 2000.
25. M. Quintard, M. Kaviany, and S. Whitaker. Two-medium treatment of heat transfer in porous media: numerical results for effective properties. *Advances in Water Resources*, 20(2–3): 77–94, April 1997. ISSN 0309-1708. .
26. David Geb, Feng Zhou, and Ivan Catton. Internal Heat Transfer Coefficient Determination in a Packed Bed From the Transient Response Due to Solid Phase Induction Heating. *Journal of Heat Transfer*, 134(4):042604–042604, February 2012. ISSN 0022-1481. .
27. Alexandre Lapene, Gerald Debenest, Michel Quintard, Martio Martins, and Sylvain Salvador. Numerical Simulation of Combustion in Reactive Porous Media. *IREME*, 12, 2008.
28. A Bejan. *Convective Heat Transfer*. 1984.
29. Nihad Dukhan, Özer Bağcı, and Mustafa Özdemir. Experimental flow in various porous media and reconciliation of Forchheimer and Ergun relations. *Experimental Thermal and Fluid Science*, 57:425–433, September 2014. ISSN 0894-1777. .
30. G Chauveteau and C Thirriot. *Sur les pertes de charge en écoulement laminaire dans quelques géométries simple et dans le milieu poreux*. Trieste edition, 1965.
31. Erik Skjetne and Jean-Louis Auriault. High-Velocity Laminar and Turbulent Flow in Porous Media. *Transport in Porous Media*, 36(2):131–147, August 1999. ISSN 0169-3913, 1573-1634. .
32. Cyprien Soulaine and Michel Quintard. On the use of a Darcy–Forchheimer like model for a macro-scale description of turbulence in porous media and its application to structured packings. *International Journal of Heat and Mass Transfer*, 74:88–100, July 2014. ISSN 0017-9310. .
33. Wojciech Sobieski, Qiang Zhang, and Chuanyun Liu. Predicting Tortuosity for Airflow Through Porous Beds Consisting of Randomly Packed Spherical Particles. *Transport in Porous Media*, 93(3):431–451, July 2012. ISSN 0169-3913, 1573-1634. .
34. M. W Chase, United States, and National Bureau of Standards. *NIST-JANAF Themochemical Tables*. American Chemical Society ; American Institute of Physics for the National Bureau of Standards, Washington, D.C.; New York, fourth edition edition, 1998.
35. Thermal Ceramics. *Organic RCF Vacuum Formed Products*.
36. John C. Chen and Stuart W. Churchill. Radiant heat transfer in packed beds. *AIChE Journal*, 9(1):35–41, January 1963. ISSN 1547-5905. .
37. N.Kh Zimina. Thermal Conductivity of Nitrogen at High Temperatures. *Teplofiz.Vys.Temp*, (2):869–878, 1964.
38. M Gupta, J Yang, and C Roy. Specific heat and thermal conductivity of softwood bark and softwood char particles. *Fuel*, 82(8):919–927, May 2003. ISSN 0016-2361. . WOS:000182003900006.
39. Alexandre Lapene, Gérald Debenest, Michel Quintard, Louis M. Castanier, Margot G. Gerritsen, and Anthony R. Kovscek. Kinetics Oxidation of Heavy Oil. 2. Application of Genetic Algorithm for Evaluation of Kinetic Parameters. *Energy & Fuels*, 29(2):1119–1129, February 2015. ISSN 0887-0624. .
40. Gabriel Teixeira, Sylvain Salvador, and Laurent Van de Steene. *Gazéification de charbon de granules de bois : comportement thermochimique et mécanique d'un lit fixe continu*. PhD thesis, INP Toulouse, Toulouse, 2012.
41. M.A. Field, D.W. Gill, B.B. Morgan, and P.G.W. Hawksley. Combustion of pulverizedfuel. *British Coam Utilizatioon Research Association*, pages 155–173, 1967.
42. M. Sennoune, S. Salvador, and G. Debenest. Impact of a CO2-Enriched Gas on the Decarbonation of CaCO3 and the Oxidation of Carbon in the Smoldering Process of Oil Shale Semicoke. *Energy & Fuels*, 26(1):391–399, January 2012. ISSN 0887-0624. . WOS:000299583400042.
43. S. M. White and Prof C. L. Tien. Analysis of flow channeling near the wall in packed beds. *Wärme - und Stoffübertragung*, 21(5):291–296, September 1987. ISSN 0042-9929, 1432-1181. .